Detailed calculation of lepton flavor violating muon-electron conversion rate for various nuclei

Ryuichiro Kitano*
Theory Group, KEK, Oho 1-1, Tsukuba, Ibaraki 305-0801, Japan
and Department of Particle and Nuclear Physics, The Graduate University for Advanced Studies, Oho 1-1, Tsukuba, Ibaraki 305-0801, Japan

Masafumi Koike†
Theory Group, KEK, Oho 1-1, Tsukuba, Ibaraki 305-0801, Japan

Yasuhiro Okada‡
Theory Group, KEK, Oho 1-1, Tsukuba, Ibaraki 305-0801, Japan
and Department of Particle and Nuclear Physics, The Graduate University for Advanced Studies, Oho 1-1, Tsukuba, Ibaraki 305-0801, Japan

(Received 13 March 2002; revised manuscript received 20 August 2002; published 6 November 2002)

The coherent μ-e conversion rates in various nuclei are calculated for general lepton flavor violating interactions. We solve the Dirac equations numerically for the initial state muon and the final state electron in the Coulomb force, and perform the overlap integrations between the wave functions and the nucleon densities. The results indicate that the conversion branching ratio increases for a light nucleus up to the atomic number $Z\sim 30$, is largest for $Z=30$–60, and becomes smaller for a heavy nucleus with $Z\gtrsim 60$. We also discuss the uncertainty from the input proton and neutron densities. The atomic number dependence of the conversion ratio calculated here is useful to distinguish theoretical models with lepton flavor violation.

DOI: 10.1103/PhysRevD.66.096002 PACS number(s): 11.30.Fs, 14.60.Ef

I. INTRODUCTION

The observation of lepton flavor violation (LFV) is one of the most interesting signals beyond the standard model (SM). Charged-lepton LFV processes such as $\mu\to e\gamma$ decay and μ-e conversion in muonic atoms can occur in many promising candidates beyond the SM, although the simple seesaw neutrino model does not induce an experimentally observable rate for the $\mu\to e\gamma$ process. For example, sleptons in the supersymmetric (SUSY) extension of the SM and bulk neutrinos in the higher dimensional models generate LFV processes through one-loop diagrams [1,2]. In *R*-parity violating SUSY models, additional LFV interactions exist at the tree level [3]. The branching ratios of the LFV processes have been calculated in many models in the literature, especially for supersymmetric grand unified theories (SUSY GUTs) [4,5] and a SUSY model with right-handed neutrinos [6]. It was shown that $\mu\to e\gamma$ and μ-e conversion branching ratios can be close to the experimental bounds in these models.

There are ongoing and planned experiments for $\mu\to e\gamma$ and μ-e conversion searches. For the $\mu\to e\gamma$ branching ratio, the present upper bound is 1.2×10^{-11} from the MEGA Collaboration [7]. A new experiment is under construction at PSI aiming for a sensitivity of 10^{-14} [8]. For the μ-e conversion, an upper bound for the conversion branching ratio is 6.1×10^{-13} [9] reported by the SINDRUM II experiment at PSI. Now SINDRUM II is running with gold (Au) targets. The MECO experiment at BNL [10] is planned to search for $\mu\mathrm{Al}\to e\mathrm{Al}$ with a sensitivity below 10^{-16}. In the future, further improvements by one or two orders of magnitude are under consideration for both $\mu\to e\gamma$ and μ-e conversion processes in the PRISM project [11] at the new 50 GeV proton synchrotron constructed as a part of the JAERI-KEK joint project.

In order to compare the sensitivity to the LFV interaction in various nuclei, a precise calculation of the μ-e conversion rate is necessary. There have been several calculations of the conversion rate. Weinberg and Feinberg considered the case that the conversion occurs through photonic interactions (μ-e-γ vertex) [12]. In the calculation, they used several approximations in which the muon wave function was taken to be constant in a nucleus and the outgoing electron was treated as a plane wave. The plane wave treatment of the electron is a good approximation only for light nuclei because the effect of Coulomb distortion on the electron wave function is large for heavy targets. The nonphotonic interaction case was studied by Marciano and Sanda [13]. Shanker improved the calculation by solving the Dirac equations for the muon and electron wave functions in the electric potential of a nucleus [14]. The calculation was carried out for all the interactions including the photonic and four-fermion operators in the effective Lagrangian, but the treatment of the photonic dipole operator was incomplete because he used the approximation that off-shell photon exchange was replaced by a four-fermion interaction. Recently, Czarnecki *et al.* presented a calculation in which the off-shell photon is properly treated as an electric field in the nucleus and listed the values of the conversion rate for aluminum (Al), titanium (Ti), and lead (Pb) targets [15]. The transition rates to the ground state of a nucleus as well as excited states are calculated in Refs. [16,17].

*Email address: ryuichiro.kitano@kek.jp
†Email address: mkoike@post.kek.jp
‡Email address: yasuhiro.okada@kek.jp

In this paper, we evaluated the μ-e conversion rates for nuclei of a wide range of atomic numbers by the method of Czarnecki *et al*. We took into account all the operators for the μ-e transition. For any type of operator, the results of our calculation indicate a tendency for the conversion branching ratio to be larger for nuclei with moderate atomic numbers than for light or heavy nuclei. Although the tendency is the same, there are significant differences in the Z dependence of the conversion rate for various LFV couplings. Experiments in various nuclei are therefore useful for model discrimination because each theoretical model predicts different Z dependences. The conversion rate depends on the input proton and neutron densities for each nucleus. Although the proton density is well measured by electron scattering, there is uncertainty in the determination of neutron densities. We estimate the uncertainty from these input parameters. Based on the neutron density distribution determined from proton scattering experiments performed in the 1970s and pionic atom experiments, the conversion rate changes by 20%–30% for heavy nuclei. The ambiguity is shown to be significantly reduced for lead (Pb) by the improved determination of the neutron density from a new proton scattering experiment.

This paper is organized as follows. In Sec. II, we present a formula of the conversion rate with the most general effective Lagrangian for LFV. The results of our calculation and the estimation of the uncertainty are shown in Sec. III. In Sec. IV, we summarize this paper. The model parameters for the nucleon density functions in nuclei and the muon capture rate in nuclei are listed in Appendixes A and B, respectively.

II. FORMULA OF μ-e CONVERSION RATE

In this section, we present a method for the conversion rate calculation. We solve the Dirac equations for the muon and electron in the initial and final states, respectively, and obtain transition amplitudes by integrating the overlap of both wave functions.

We start with the most general LFV interaction Lagrangian which contributes to the μ-e transition in nuclei [1]:

$$\begin{aligned}\mathcal{L}_{\rm int}=&-\frac{4G_{\rm F}}{\sqrt{2}}(m_\mu A_R\bar{\mu}\sigma^{\mu\nu}P_L eF_{\mu\nu}+m_\mu A_L\bar{\mu}\sigma^{\mu\nu}P_R eF_{\mu\nu}+\text{H.c.})-\frac{G_{\rm F}}{\sqrt{2}}\sum_{q=u,d,s}\Big[(g_{LS(q)}\bar{e}P_R\mu+g_{RS(q)}\bar{e}P_L\mu)\bar{q}q\\&+(g_{LP(q)}\bar{e}P_R\mu+g_{RP(q)}\bar{e}P_L\mu)\bar{q}\gamma_5 q+(g_{LV(q)}\bar{e}\gamma^\mu P_L\mu+g_{RV(q)}\bar{e}\gamma^\mu P_R\mu)\bar{q}\gamma_\mu q+(g_{LA(q)}\bar{e}\gamma^\mu P_L\mu\\&+g_{RA(q)}\bar{e}\gamma^\mu P_R\mu)\bar{q}\gamma_\mu\gamma_5 q+\frac{1}{2}(g_{LT(q)}\bar{e}\sigma^{\mu\nu}P_R\mu+g_{RT(q)}\bar{e}\sigma^{\mu\nu}P_L\mu)\bar{q}\sigma_{\mu\nu}q+\text{H.c.}\Big],\end{aligned}\tag{1}$$

where $G_{\rm F}$ and m_μ are the Fermi constant and the muon mass, respectively, and $A_{L,R}$ and the g's are all dimensionless coupling constants for the corresponding operators. Our conventions are $F_{\mu\nu}=\partial_\mu A_\nu-\partial_\nu A_\mu$, $\sigma^{\mu\nu}=(i/2)[\gamma^\mu,\gamma^\nu]$, $P_L=(1-\gamma_5)/2$, $P_R=(1+\gamma_5)/2$, and the covariant derivative is defined as $D_\mu=\partial_\mu-iQeA_\mu$, where Qe $(e>0)$ is the electric charge ($Q=-1$ for the electron and the muon). The size of each coupling constant depends on the interaction of new physics in which lepton flavor conservation is violated. There are two types of amplitude for the photonic transition (μ-e-γ), namely, the monopole and dipole μ-e transitions. In the above expression, the monopole transition is converted to the vector-vector interaction assuming that the momentum dependences of the form factors are negligible.

The initial state in the μ-e conversion process is the $1s$ state of the muonic atom, and the final electron state is the eigenstate with energy of $m_\mu-\epsilon_b$, where ϵ_b is the binding energy of the $1s$ muonic atom. Both wave functions in the initial and final states can be determined by solving the Dirac equations in the electric field of the nucleus. The Dirac equation in the central force system is given by [18]

$$W\psi=\left[-i\gamma_5\sigma_r\left(\frac{\partial}{\partial r}+\frac{1}{r}-\frac{\beta}{r}K\right)+V(r)+m_i\beta\right]\psi,\tag{2}$$

$$\gamma_5=\begin{pmatrix}0&1\\1&0\end{pmatrix},\quad \beta=\begin{pmatrix}1&0\\0&-1\end{pmatrix},$$

$$\sigma_r=\begin{pmatrix}\boldsymbol{\sigma}\cdot\boldsymbol{r}&0\\0&\boldsymbol{\sigma}\cdot\boldsymbol{r}\end{pmatrix},$$

$$K=\begin{pmatrix}\boldsymbol{\sigma}\cdot\boldsymbol{l}+1&0\\0&-(\boldsymbol{\sigma}\cdot\boldsymbol{l}+1)\end{pmatrix},\tag{3}$$

where W and $V(r)$ are the energy and potential, respectively, m_i is the reduced mass of the electron or the muon, $\boldsymbol{\sigma}$ are the Pauli matrices, and the orbital angular momentum $\boldsymbol{l}$ is defined by $\boldsymbol{l}\equiv-i\boldsymbol{r}\times\boldsymbol{\nabla}$. Since the operator K and the z component of the total angular momentum j_z commute with the Hamiltonian, two eigenvalues of these operators, $-\kappa$ and μ, represent the quantum numbers of the wave functions describing this system. We denote the wave function as follows:

$$\psi=\psi^\mu_\kappa=\begin{pmatrix}g(r)\chi^\mu_\kappa(\theta,\phi)\\ if(r)\chi^\mu_{-\kappa}(\theta,\phi)\end{pmatrix},\tag{4}$$

where χ^μ_κ is the normalized simultaneous eigenfunction of $(\boldsymbol{\sigma}\cdot\boldsymbol{l}+1)$ and j_z as follows:

$$(\boldsymbol{\sigma}\cdot\boldsymbol{l}+1)\chi_\kappa^\mu=-\kappa\chi_\kappa^\mu,\quad j_z\chi_\kappa^\mu=\mu\chi_\kappa^\mu,$$

$$\int_{-1}^{1}d\cos\theta\int_0^{2\pi}d\phi\chi_\kappa^{\mu*}\chi_{\kappa'}^{\mu'}=\delta_{\mu\mu'}\delta_{\kappa\kappa'}. \tag{5}$$

The total angular momentum j is related to κ as $\kappa=\pm(j+1/2)$. With the notation $u_1(r)=rg(r)$ and $u_2(r)=rf(r)$, the Dirac equation for the radial function is given by

$$\frac{d}{dr}\begin{pmatrix}u_1\\u_2\end{pmatrix}=\begin{pmatrix}-\kappa/r & W-V+m_i\\ -(W-V-m_i) & \kappa/r\end{pmatrix}\begin{pmatrix}u_1\\u_2\end{pmatrix}. \tag{6}$$

The initial muon state corresponds to the quantum numbers $\mu=\pm1/2$ and $\kappa=-1$ with a normalization of

$$\int d^3x\,\psi_{1s}^{(\mu)*}(\mathbf{x})\,\psi_{1s}^{(\mu)}(\mathbf{x})=1. \tag{7}$$

The final electron state is one of the states in the continuum spectrum. Our normalization convention is taken as

$$\int d^3x\,\psi_{\kappa,W}^{\mu(e)*}(\mathbf{x})\,\psi_{\kappa',W'}^{\mu'(e)}(\mathbf{x})=2\pi\delta_{\mu\mu'}\delta_{\kappa\kappa'}\delta(W-W'). \tag{8}$$

The conversion rate $\omega_{\rm conv}$ in this normalization is simply written by the square of the μ-e conversion amplitude M, taking the spin average of the initial muon and summing over the final states of the electron. From the effective Lagrangian (1), M is obtained as follows:

$$\begin{aligned}M=\frac{4G_{\rm F}}{\sqrt{2}}\int d^3x(&m_\mu A_R^*\bar{\psi}_{\kappa,W}^{\mu(e)}\sigma^{\alpha\beta}P_R\psi_{1s}^{(\mu)}+m_\mu A_L^*\bar{\psi}_{\kappa,W}^{\mu(e)}\sigma^{\alpha\beta}P_L\psi_{1s}^{(\mu)})\langle N'|F_{\alpha\beta}|N\rangle+\frac{G_{\rm F}}{\sqrt{2}}\sum_{q=u,d,s}\int d^3x\Big[(g_{LS(q)}\bar{\psi}_{\kappa,W}^{\mu(e)}P_R\psi_{1s}^{(\mu)}\\&+g_{RS(q)}\bar{\psi}_{\kappa,W}^{\mu(e)}P_L\psi_{1s}^{(\mu)})\langle N'|\bar{q}q|N\rangle+(g_{LP(q)}\bar{\psi}_{\kappa,W}^{\mu(e)}P_R\psi_{1s}^{(\mu)}+g_{RP(q)}\bar{\psi}_{\kappa,W}^{\mu(e)}P_L\psi_{1s}^{(\mu)})\langle N'|\bar{q}\gamma_5q|N\rangle+(g_{LV(q)}\bar{\psi}_{\kappa,W}^{\mu(e)}\gamma^\alpha P_L\psi_{1s}^{(\mu)}\\&+g_{RV(q)}\bar{\psi}_{\kappa,W}^{\mu(e)}\gamma^\alpha P_R\psi_{1s}^{(\mu)})\langle N'|\bar{q}\gamma_\alpha q|N\rangle+(g_{LA(q)}\bar{\psi}_{\kappa,W}^{\mu(e)}\gamma^\alpha P_L\psi_{1s}^{(\mu)}+g_{RA(q)}\bar{\psi}_{\kappa,W}^{\mu(e)}\gamma^\alpha P_R\psi_{1s}^{(\mu)})\langle N'|\bar{q}\gamma_\alpha\gamma_5q|N\rangle\\&+\frac{1}{2}(g_{LT(q)}\bar{\psi}_{\kappa,W}^{\mu(e)}\sigma^{\alpha\beta}P_R\psi_{1s}^{(\mu)}+g_{RT(q)}\bar{\psi}_{\kappa,W}^{\mu(e)}\sigma^{\alpha\beta}P_L\psi_{1s}^{(\mu)})\langle N'|\bar{q}\sigma_{\alpha\beta}q|N\rangle\Big],\end{aligned} \tag{9}$$

where $\langle N'|$ and $|N\rangle$ are the final and initial states of the nucleus, respectively.

Hereafter, we concentrate on the coherent conversion processes in which the final state of the nucleus is the same as the initial one. The fraction of the coherent process is generally larger than that of the incoherent one approximately by a factor of the mass number of the target nuclei. In this case, the matrix elements of $\langle N|\bar{q}\gamma_5q|N\rangle$, $\langle N|\bar{q}\gamma_\alpha\gamma_5q|N\rangle$, and $\langle N|\bar{q}\sigma_{\alpha\beta}q|N\rangle$ vanish, and $\langle N|\bar{q}q|N\rangle$ and $\langle N|\bar{q}\gamma_\alpha q|N\rangle$ can be expressed by the proton and neutron densities ($\rho^{(p)}$ and $\rho^{(n)}$) in nuclei as follows:

$$\langle N|\bar{q}q|N\rangle=ZG_S^{(q,p)}\rho^{(p)}+(A-Z)G_S^{(q,n)}\rho^{(n)}, \tag{10}$$

$$\langle N|\bar{q}\gamma^0q|N\rangle=\begin{cases}2Z\rho^{(p)}+(A-Z)\rho^{(n)} & \text{for}\quad q=u,\\ Z\rho^{(p)}+2(A-Z)\rho^{(n)} & \text{for}\quad q=d,\\ 0 & \text{for}\quad q=s,\end{cases} \tag{11}$$

$$\langle N|\bar{q}\gamma^iq|N\rangle=0\quad(i=1,2,3). \tag{12}$$

Here we introduce the coefficients $G_S^{(q,p)}$ and $G_S^{(q,n)}$ for scalar operators. These were evaluated as $G_S^{(u,p)}=G_S^{(d,n)}=5.1$, $G_S^{(d,p)}=G_S^{(u,n)}=4.3$, and $G_S^{(s,p)}=G_S^{(s,n)}=2.5$ by Kosmas *et al.* [19]. We assume that the proton and neutron densities are spherically symmetric and normalized as follows:

$$\int_0^\infty dr\,4\pi r^2\rho^{(p,n)}(r)=1. \tag{13}$$

The final formula for the conversion rate can be written as follows:

$$\begin{aligned}\omega_{\rm conv}=2G_{\rm F}^2|&A_R^*D+\tilde{g}_{LS}^{(p)}S^{(p)}+\tilde{g}_{LS}^{(n)}S^{(n)}\\&+\tilde{g}_{LV}^{(p)}V^{(p)}+\tilde{g}_{LV}^{(n)}V^{(n)}|^2+2G_{\rm F}^2|A_L^*D+\tilde{g}_{RS}^{(p)}S^{(p)}\\&+\tilde{g}_{RS}^{(n)}S^{(n)}+\tilde{g}_{RV}^{(p)}V^{(p)}+\tilde{g}_{RV}^{(n)}V^{(n)}|^2.\end{aligned} \tag{14}$$

A_L and A_R are given in Eq. (1). The coupling constants $\tilde{g}$ in Eq. (14) are defined as

$$\tilde{g}_{LS,RS}^{(p)}=\sum_q G_S^{(q,p)}g_{LS,RS(q)}, \tag{15}$$

$$\tilde{g}_{LS,RS}^{(n)}=\sum_q G_S^{(q,n)}g_{LS,RS(q)}, \tag{16}$$

$$\tilde{g}_{LV,RV}^{(p)}=2g_{LV,RV(u)}+2g_{LV,RV(d)}, \tag{17}$$

$$\tilde{g}_{LV,RV}^{(n)}=g_{LV,RV(u)}+2g_{LV,RV(d)}. \tag{18}$$

We also introduced the following overlap integrals:

$$D=\frac{4}{\sqrt{2}}m_\mu\int_0^\infty drr^2[-E(r)](g_e^- f_\mu^- + f_e^- g_\mu^-), \tag{19}$$

$$S^{(p)}=\frac{1}{2\sqrt{2}}\int_0^\infty drr^2 Z\rho^{(p)}(g_e^- g_\mu^- - f_e^- f_\mu^-), \tag{20}$$

$$S^{(n)}=\frac{1}{2\sqrt{2}}\int_0^\infty drr^2 (A-Z)\rho^{(n)}(g_e^- g_\mu^- - f_e^- f_\mu^-), \tag{21}$$

$$V^{(p)}=\frac{1}{2\sqrt{2}}\int_0^\infty drr^2 Z\rho^{(p)}(g_e^- g_\mu^- + f_e^- f_\mu^-), \tag{22}$$

$$V^{(n)}=\frac{1}{2\sqrt{2}}\int_0^\infty drr^2 (A-Z)\rho^{(n)}(g_e^- g_\mu^- + f_e^- f_\mu^-), \tag{23}$$

where the functions g_e^-, etc., are defined in the $1s$ muon wave function and $\kappa=\pm 1$ electron wave functions as follows:

$$\psi_{1s}^{(\mu)}(r,\theta,\phi)=\begin{pmatrix} g_\mu^-(r)\chi_{-1}^{\pm 1/2}(\theta,\phi) \\ if_\mu^-(r)\chi_1^{\pm 1/2}(\theta,\phi)\end{pmatrix}, \tag{24}$$

$$\psi_{\kappa=-1,W}^{\mu=\pm 1/2(e)}(r,\theta,\phi)=\begin{pmatrix} g_e^-(r)\chi_{-1}^{\pm 1/2}(\theta,\phi) \\ if_e^-(r)\chi_1^{\pm 1/2}(\theta,\phi)\end{pmatrix}, \tag{25}$$

$$\psi_{\kappa=1,W}^{\mu=\pm 1/2(e)}(r,\theta,\phi)=\begin{pmatrix} g_e^+(r)\chi_1^{\pm 1/2}(\theta,\phi) \\ if_e^+(r)\chi_{-1}^{\pm 1/2}(\theta,\phi)\end{pmatrix}. \tag{26}$$

In the above expressions, we have neglected the electron mass, so that g_e^+ and f_e^+ are related to g_e^- and f_e^- as $g_e^+ = if_e^-$ and $if_e^+ = g_e^-$. By integrating the Maxwell equations, the electric field $E(r)$ is determined as

$$E(r)=\frac{Ze}{r^2}\int_0^r r'^2\rho^{(p)}(r')dr'. \tag{27}$$

Once the proton and neutron densities are given, one can calculate the electric field $E(r)$ by Eq. (27) and the electric potential $V(r)$ by

$$V(r)=-e\int_r^\infty E(r')dr'. \tag{28}$$

The wave functions are then obtained by the Dirac equation Eq. (6), and the μ-e conversion rate is calculated by Eq. (14).

III. NUMERICAL RESULTS

In order to evaluate Eq. (14), we need proton and neutron densities and the muon and electron wave functions. We first discuss proton and neutron densities and show the wave functions of the muon and electron. Then we present numerical results of the overlap integrals Eqs. (19)–(23) and the conversion rates for various nuclei.

A. Distribution of protons and neutrons in the nucleus

We have used proton densities determined from electron scattering experiments. In the past, the charge density distribution of a nucleus was analyzed assuming some functional form of the proton distribution such as the two-parameter Fermi model, the three-parameter Fermi model, and the three-parameter Gaussian model. More recently, with improvement of experimental data, model-independent methods have been used to extract detailed information on the density distribution. Examples are the Fourier-Bessel expansion and the sum of Gaussian functions. The proton density is very precisely determined when a model-independent analysis is carried out. We use the charge density listed in Ref. [20]. We adopt the results of model-independent analyses when the data are available. More detail of the charge distribution is described in Appendix A.

The determination of the neutron distribution is not as easy as that of the proton distribution [21]. There are several ways to determine the neutron density in the different regions. Pionic atoms provide a probe of the neutron density on the periphery of the nucleus. In a certain level of the pionic atom the pion is absorbed by the nucleus. Since the strong interaction between the pion and the nucleus changes the energy and the width of this level, we can obtain information on the neutron density in the nucleus from analysis of the atomic x-ray spectrum. Scattering experiments on the nucleus by strong interacting particles such as the proton, the alpha particle, and the charged pion are also useful to determine the neutron density. Recently, an experiment with antiprotonic atoms was carried out to determine the proton and neutron density distributions in the periphery region of various nuclei [22].

In this paper we use the following three methods to evaluate the μ-e conversion ratio.

Method 1. First, we take the proton density from electron scattering experiments given in Appendix A and assume that the neutron density is the same as the proton density. For light nuclei this is a good approximation because the numbers of neutrons and protons are approximately equal and the conversion rates do not depend on the details of the neutron distribution.

Method 2. Second, we employ the neutron distribution obtained from the pionic atom. We use the results of the analysis of Ref. [23], where the proton and neutron distributions are given in terms of the two-parameter Fermi function.

Method 3. Finally, we use the neutron distribution obtained from the polarized proton scattering experiment. The analysis was carried out for carbon (C) [24], titanium (Ti) [25], nickel (Ni) [24], zirconium (Zr) [24], and lead (Pb) [24], where the proton and neutron density are given in the literature. We also estimate the uncertainty due to the error of the neutron distribution from the scattering experiment based on Refs. [26–28].

The first method gives a precise evaluation of the overlap integrals D, $S^{(p)}$, and $V^{(p)}$. On the other hand, the neutron density is necessary in order to determine $S^{(n)}$ and $V^{(n)}$. Since both methods 2 and 3 use strongly interacting particles as probes of the neutron density, the calculation suffers from ambiguities associated with the pion/proton-nucleon interac-

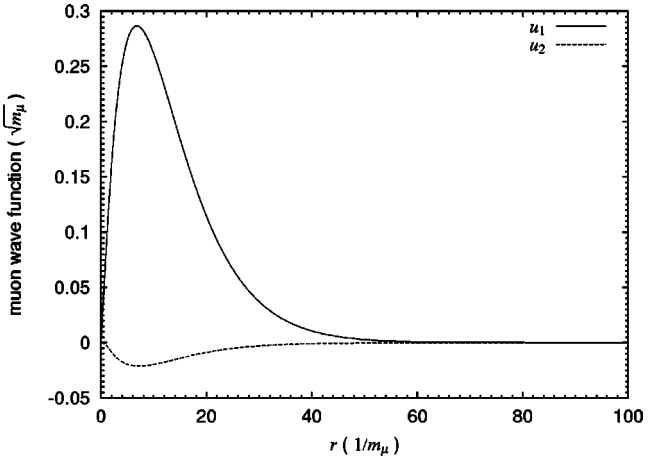

FIG. 1. The normalized wave function of a muon in the titanium (Ti) nucleus is plotted. The solid line and dashed line represent u_1 ($\equiv r g_\mu^-$) and u_2 ($\equiv r f_\mu^-$) components, respectively. The horizontal axis is the distance between the nucleus and the muon in units of $1/m_\mu$. The unit for the wave function is taken to be $\sqrt{m_\mu}$.

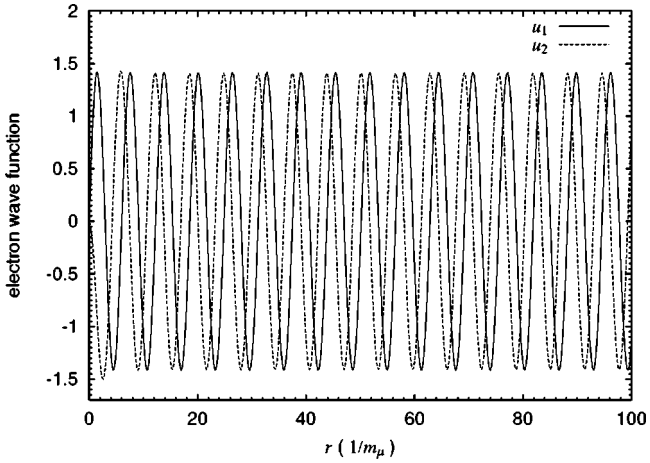

FIG. 2. The normalized wave function of an electron in the titanium (Ti) nucleus is plotted. The solid line and dashed line represent u_1 ($\equiv r g_e^-$) and u_2 ($\equiv r f_e^-$) components, respectively. The horizontal axis is the distance between the nucleus and the electron in units of $1/m_\mu$.

tion. Method 2 provides information on the size of the nucleus in a wide range of atomic numbers. On the other hand, we can determine in method 3 the profile of the neutron distribution inside the nucleus for selected nuclei. We calculate the conversion rate by two methods, and first discuss the ambiguities in each method and then compare the results.

B. Numerical evaluation of the overlap integrals

In this subsection, we first show an example of the muon and electron wave functions obtained by solving the Dirac equation Eq. (2), and present the results of a numerical calculation of the overlap integrals D, $S^{(p,n)}$, and $V^{(p,n)}$ defined by Eqs. (19)–(23).

1. Wave functions of the initial and final states

The muon and electron wave functions are evaluated by solving the Dirac equation (2) with the electric potential given by Eq. (28). Ignoring the recoil of the nucleus, which is of the order of m_μ^2/M_N, where M_N is the nucleus mass, one finds that the energy of the outgoing electron in Eq. (2) is equal to the muon mass minus the binding energy. As an example, we show the muon and electron wave functions in the titanium (Ti) nucleus in Figs. 1 and 2. We can see in Fig. 1 that the lower component u_2 in the muon wave function is much smaller than the upper component u_1. However, as pointed out in Ref. [14], its effect on the conversion rate is sizable for heavy nuclei. The overlap integrals are evaluated using these wave functions.

2. Method 1

We present in Table I the results under the assumption $\rho_n = \rho_p$, where ρ_p is taken from Ref. [20]. We show in Fig. 3 the Z dependence of the integrals. We omitted the points for $^{166}_{68}$Er, $^{181}_{73}$Ta, and $^{197}_{79}$Au from this figure since these data are either obtained from quite old experiments or not well established [20]. We see that the overlap integrals increase as functions of Z for light nuclei up to $Z \sim 30$, and saturate or decrease for heavy nuclei.

Although the tendency is the same, each overlap integral has a different Z dependence, especially for heavy nuclei. For example, the scalar ($S^{(p,n)}$) and the vector ($V^{(p,n)}$) type integrals are almost equal in light nuclei ($Z \lesssim 30$), whereas the vectorlike integral is larger by a factor of 1.5–2 than the scalar one for heavy nuclei. This difference is due to the relativistic effects of the muon wave functions, which are significant in heavy nuclei. In fact, the scalar and vector overlap integrals in Eqs. (20) and (22) [Eqs. (21) and (23)] are exactly the same if we ignore the small component of the wave function f_μ^-. For D we can show that $D/(8e) \simeq S^{(p)} \simeq V^{(p)}$ is satisfied for light nuclei.

The qualitative features of the Z dependence of the overlap integrals can be understood from the following considerations. When we adopt the approximation of Weinberg and Feinberg [12], where the muon wave function is replaced by the average value and the electron wave function is treated as a plane wave, the formulas for the overlap integrals in Eqs. (20) and (22) are given by

$$V^{(p)} \sim S^{(p)} \sim \frac{1}{8\pi} \langle \phi_\mu \rangle Z F_p . \tag{29}$$

Here F_p is the form factor defined by

$$F_p = \int_0^\infty dr\, 4\pi r^2 \rho^{(p)} \frac{\sin m_\mu r}{m_\mu r}, \tag{30}$$

and $\langle \phi_\mu \rangle$ is the average value of the muon wave function in the nucleus given by

$$\langle \phi_\mu \rangle^2 = \int_0^\infty dr\, 4\pi r^2 (g_\mu^2 + f_\mu^2) \rho^{(p)} = \frac{4 m_\mu^3 \alpha^3 Z_{\rm eff}^4}{Z}. \tag{31}$$

TABLE I. The overlap integrals in units of $m_\mu^{5/2}$ are listed. The proton distributions in the nuclei are taken from Ref. [20] (see also Appendix A), and neutron distributions are assumed to be the same as those of the protons (method 1 in Sec. III A).

Nucleus	D	$S^{(p)}$	$V^{(p)}$	$S^{(n)}$	$V^{(n)}$
$^{4}_{2}$He	0.000625	0.000262	0.000263	0.000262	0.000263
$^{7}_{3}$Li	0.00138	0.000581	0.000585	0.000775	0.000780
$^{9}_{4}$Be	0.00268	0.00113	0.00114	0.00141	0.00142
$^{11}_{5}$B	0.00472	0.00200	0.00202	0.00240	0.00242
$^{12}_{6}$C	0.00724	0.00308	0.00312	0.00308	0.00312
$^{14}_{7}$N	0.0103	0.0044	0.0044	0.0044	0.0044
$^{16}_{8}$O	0.0133	0.0057	0.0058	0.0057	0.0058
$^{19}_{9}$F	0.0166	0.0071	0.0072	0.0079	0.0081
$^{20}_{10}$Ne	0.0205	0.0088	0.0090	0.0088	0.0090
$^{24}_{12}$Mg	0.0312	0.0133	0.0138	0.0133	0.0138
$^{27}_{13}$Al	0.0362	0.0155	0.0161	0.0167	0.0173
$^{28}_{14}$Si	0.0419	0.0179	0.0187	0.0179	0.0187
$^{31}_{15}$P	0.0468	0.0201	0.0210	0.0214	0.0224
$^{32}_{16}$S	0.0524	0.0225	0.0236	0.0225	0.0236
$^{35}_{17}$Cl	0.0565	0.0241	0.0254	0.0256	0.0269
$^{40}_{18}$Ar	0.0621	0.0265	0.0281	0.0324	0.0343
$^{39}_{19}$K	0.0699	0.0299	0.0317	0.0314	0.0334
$^{40}_{20}$Ca	0.0761	0.0325	0.0347	0.0325	0.0347
$^{48}_{22}$Ti	0.0864	0.0368	0.0396	0.0435	0.0468
$^{51}_{23}$V	0.0931	0.0396	0.0428	0.0482	0.0521
$^{52}_{24}$Cr	0.100	0.0425	0.0461	0.0496	0.0538
$^{55}_{25}$Mn	0.107	0.0456	0.0496	0.0547	0.0596
$^{56}_{26}$Fe	0.110	0.0467	0.0512	0.0539	0.0591
$^{59}_{27}$Co	0.112	0.0471	0.0519	0.0558	0.0615
$^{58}_{28}$Ni	0.125	0.0527	0.0583	0.0565	0.0625
$^{63}_{29}$Cu	0.122	0.0514	0.0572	0.0603	0.0671
$^{64}_{30}$Zn	0.134	0.0561	0.0627	0.0636	0.0710
$^{74}_{32}$Ge	0.133	0.0554	0.0628	0.0727	0.0824
$^{80}_{34}$Se	0.146	0.0602	0.0690	0.0815	0.0933
$^{88}_{38}$Sr	0.163	0.0665	0.0778	0.0875	0.102
$^{89}_{39}$Y	0.164	0.0670	0.0788	0.0859	0.101
$^{90}_{40}$Zr	0.171	0.0697	0.0823	0.0872	0.103
$^{93}_{41}$Nb	0.171	0.0692	0.0823	0.0878	0.104
$^{98}_{42}$Mo	0.170	0.0683	0.0818	0.0911	0.109
$^{110}_{46}$Pd	0.176	0.0695	0.0855	0.0967	0.119
$^{114}_{48}$Cd	0.178	0.0696	0.0867	0.0958	0.119
$^{115}_{49}$In	0.181	0.0704	0.0882	0.0948	0.119
$^{120}_{50}$Sn	0.183	0.0707	0.0894	0.0990	0.125
$^{121}_{51}$Sb	0.195	0.0760	0.0957	0.104	0.131
$^{138}_{56}$Ba	0.184	0.0688	0.0911	0.101	0.133
$^{139}_{57}$La	0.189	0.0707	0.0937	0.102	0.135
$^{142}_{60}$Nd	0.183	0.0669	0.0909	0.0914	0.124
$^{152}_{62}$Sm	0.175	0.0631	0.0875	0.0915	0.127
$^{158}_{64}$Gd	0.173	0.0613	0.0865	0.0901	0.127
$^{165}_{67}$Ho	0.177	0.0617	0.0892	0.0902	0.131
$^{166}_{68}$Er	0.200	0.0693	0.101	0.0999	0.146
$^{181}_{73}$Ta	0.156	0.0513	0.0792	0.0759	0.117
$^{184}_{74}$W	0.156	0.0499	0.0794	0.0741	0.118
$^{197}_{79}$Au	0.189	0.0614	0.0974	0.0918	0.146
$^{204}_{80}$Hg	0.158	0.0482	0.0818	0.0746	0.127

TABLE I. (*Continued*).

Nucleus	D	$S^{(p)}$	$V^{(p)}$	$S^{(n)}$	$V^{(n)}$
$^{205}_{81}$Tl	0.161	0.0491	0.0834	0.0752	0.128
$^{208}_{82}$Pb	0.161	0.0488	0.0834	0.0749	0.128
$^{209}_{83}$Bi	0.159	0.0475	0.0826	0.0722	0.125
$^{232}_{90}$Th	0.154	0.0429	0.0809	0.0677	0.128
$^{238}_{92}$U	0.151	0.0417	0.0798	0.0662	0.127

In the last expression, we have introduced $Z_{\rm eff}$, which is the effective charge for the muon in the $1s$ state. We show $Z_{\rm eff}$ in Fig. 4. Since the muon wave function enters inside the nucleus, $Z_{\rm eff}$ does not increase linearly with respect to Z. In Fig. 5, we show the form factor F_p calculated based on method 1. There we see that F_p is a decreasing function of Z and suppressed for heavy nuclei. These two properties explain the Z dependence of the overlap integrals.

3. Method 2

We present in Table II and Fig. 6 the values of the overlap integrals in method 2, in which the input nucleon distributions are obtained from analysis of the pionic atom experiments [23]. In this method, the proton and neutron densities are given in the form of the two-parameter Fermi model defined by Eq. (A2) in Appendix A. Using the energy shift and the decay width of the pionic atom, the neutron density is determined together with parameters in the pion-nucleon optical potential. In Ref. [23], it is assumed that the diffuseness of the neutron density is the same as that of the proton density, $z_n = z_p$, so that the output parameter is the radius of the neutron density. For our calculation, we use the neutron matter parameter R_n[mean] in Table 4 of Ref. [23]. The Z dependence shown in Fig. 6 is similar to that seen in Fig. 3.

In order to estimate the ambiguity within this method, we have calculated $S^{(n)}$ and $V^{(n)}$ by changing the radius of the neutron density c_n within the error given in Ref. [23]. We show the results for $^{27}_{13}$Al, $^{142}_{58}$Ce, and $^{208}_{82}$Pb corresponding to light, intermediate, and heavy nuclei in Table III. The error of c_n includes the statistical error as well as the systematic error estimated from the outputs in two different parametrizations of the optical potential [23]. We see that $S^{(n)}$ and $V^{(n)}$ change $\pm 2\%$ for $^{27}_{13}$Al, $\pm(6-8)\%$ for $^{142}_{58}$Ce, and $\pm(7-11)\%$ for $^{208}_{82}$Pb.

4. Method 3

The neutron densities for selected nuclei were determined from the 800 MeV polarized proton elastic scattering experiments performed at LAMPF in the late 1970s. In Refs. [24,25], proton and neutron densities are given assuming the three-parameter Fermi or Gaussian model. Errors of the neutron distributions are estimated in a model-independent fashion in Refs. [26,27]. More recently, the determination of the neutron density has been improved for lead (Pb) based on a new experiment and a new analysis [28,29].

We calculate the overlap integrals using the neutron distribution given in the above references. Table IV and Fig. 7 show the results for the five nuclei from the Refs. [24,25]. In order to evaluate the uncertainty from the neutron distribution determined by the proton experiments, we take several examples where the error of the neutron distribution is explicitly given in the literature. We calculated $S^{(n)}$ and $V^{(n)}$ within the uncertainty of the neutron distribution. For example, we present the error band of the neutron distribution in the nucleus $^{208}_{82}$Pb in Fig. 8 [28]. Similar error bands based on older experiments are given in Ref. [26] for $^{40}_{20}$Ca, $^{58}_{28}$Ni, and $^{116}_{50}$Sn, and in Ref. [27] for $^{208}_{82}$Pb. The overlap integrals evaluated using the minimum and maximum values of the

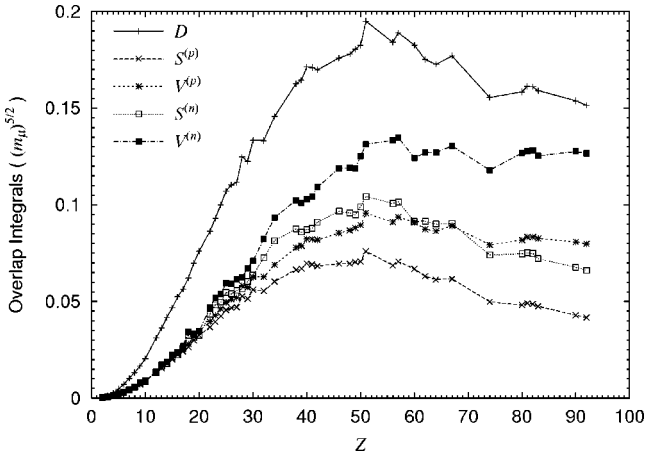

FIG. 3. The overlap integrals are plotted as functions of the atomic number Z. Neutron density distributions are assumed to be equal to charge density distributions (method 1 in Sec. III A).

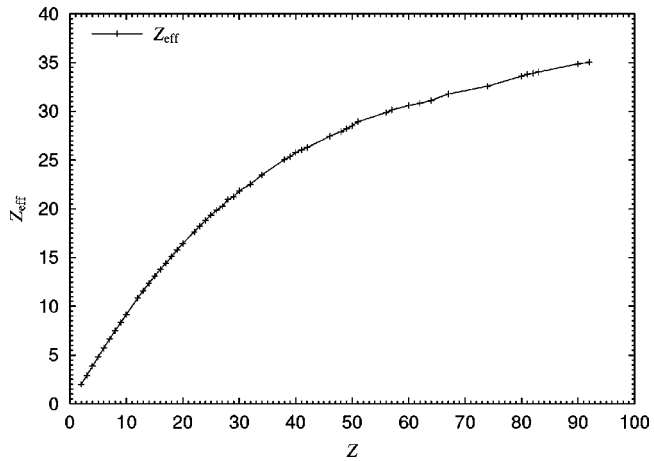

FIG. 4. The effective charge for the muon in the $1s$ state is plotted as a function of the atomic number Z.

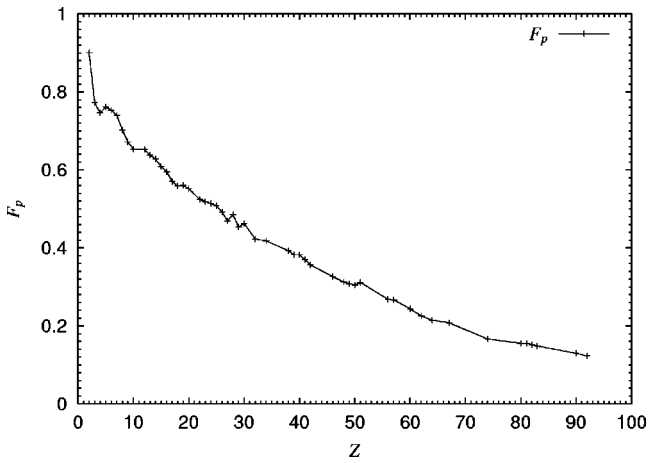

FIG. 5. The form factor F_p is plotted as a function of the atomic number Z.

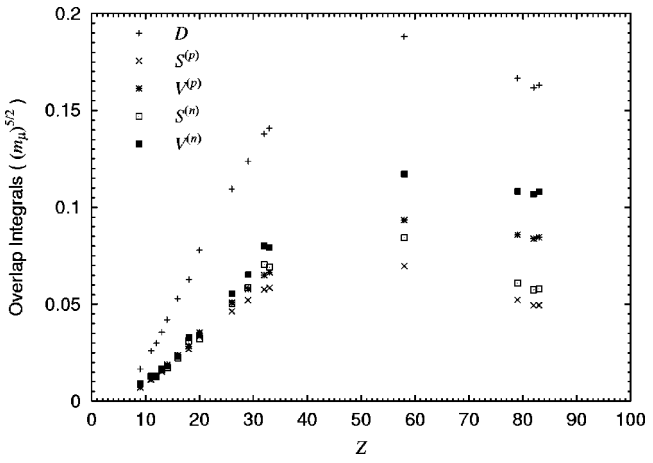

FIG. 6. Same as Fig. 3, but here the results of the analysis of the pionic atom experiment are used for the distribution of the neutrons [23] (method 2 in Sec. III A).

envelope are shown in Tables V and VI. Since the proton distribution is not explicitly given except for the case of $^{208}_{82}$Pb in Ref. [28], we use the proton distribution listed in Table VII for other cases. The errors of $S^{(n)}$ and $V^{(n)}$ amount to a few percent for light nuclei such as $^{40}_{20}$Ca and $^{58}_{28}$Ni. For $^{208}_{82}$Pb, we can see drastic improvements in the determination of $S^{(n)}$ and $V^{(n)}$ based on the new measurement. According to Ref. [28], the reduction of the errors in the neutron distribution is mainly due to higher statistical accuracy in the new experiment. This implies that improvement in proton scattering is important to determine neutron densities more precisely and reduce the ambiguity in the calculation of the μ-e conversion rate for heavy nuclei.

5. Comparison of the results by the three methods

Comparing Tables I, II, and IV, one finds that the overlap integrals of the light nuclei agree with one another within a few percent. For heavy nuclei, method 1 is not necessarily a good approximation for $S^{(n)}$ and $V^{(n)}$. However, we see that the results are consistent with the values in method 3 within 10%. Comparing methods 2 and 3, the pionic atom method gives generally smaller values by 10–20 % than the analysis based on proton scattering for intermediate and heavy nuclei.

We should note that the present analysis with pionic atoms assumes the two-parameter Fermi model with $z_p = z_n$ for neutron distributions. In Ref. [22], the neutron distribution is analyzed from an antiprotonic atom experiment, namely, nuclear spectroscopy analysis of antiproton annihilation residues and measurements of strong-interaction effects on antiprotonic x rays. The authors compared two neutron distributions of neutron skin type ($z_n = z_p$ and $c_n > c_p$) and halo type ($z_n > z_p$ and $c_n = c_p$), and concluded that the halo type distribution was favored.

In order to illustrate how the results depend on the assumption of the neutron distribution, we calculate the $S^{(n)}$ and $V^{(n)}$ in the halo type distribution with fixed values of the mean square radius. For lead (Pb), $S^{(n)}$ ($V^{(n)}$) increases by 22% (12%) compared to the skin type distribution, so that the results are very close to the values in method 3. This indicates that the overlap integrals are sensitive to the neutron distribution inside the nucleus, not only to global quantities such as the mean square radius. In method 2, the pionic atom data provide us with information on the neutron distribution mostly in the peripheral region, and therefore the interior neutron distribution is given by an extrapolation based

TABLE II. Same as Table I, but here the results of the analysis of the pionic atom experiment are used for the distribution of the neutrons [23] (method 2 in Sec. III A).

Nucleus	D	$S^{(p)}$	$V^{(p)}$	$S^{(n)}$	$V^{(n)}$
$^{19}_{9}$F	0.0166	0.0071	0.0072	0.0089	0.0090
$^{23}_{11}$Na	0.0260	0.0111	0.0114	0.0128	0.0131
$^{24}_{12}$Mg	0.0299	0.0128	0.0132	0.0126	0.0131
$^{27}_{13}$Al	0.0357	0.0153	0.0159	0.0163	0.0169
$^{28}_{14}$Si	0.0421	0.0181	0.0188	0.0173	0.0180
$^{32}_{16}$S	0.0529	0.0227	0.0238	0.0221	0.0233
$^{40}_{18}$Ar	0.0628	0.0268	0.0284	0.0310	0.0330
$^{40}_{20}$Ca	0.0778	0.0333	0.0355	0.0319	0.0341
$^{56}_{26}$Fe	0.110	0.0464	0.0508	0.0503	0.0555
$^{63}_{29}$Cu	0.124	0.0521	0.0579	0.0585	0.0654
$^{74}_{32}$Ge	0.138	0.0576	0.0651	0.0704	0.0802
$^{75}_{33}$As	0.141	0.0585	0.0665	0.0690	0.0792
$^{142}_{58}$Ce	0.188	0.0698	0.0934	0.0844	0.117
$^{197}_{79}$Au	0.167	0.0523	0.0859	0.0610	0.108
$^{208}_{82}$Pb	0.162	0.0495	0.0838	0.0575	0.107
$^{209}_{83}$Bi	0.163	0.0495	0.0846	0.0579	0.108

TABLE III. Error of the overlap integrals associated with the input value of the neutron radii determined by the pionic atom experiment. The larger (smaller) values of $S^{(n)}$ and $V^{(n)}$ correspond to smaller (larger) values of c_n.

Nucleus	c_n (fm)	$S^{(n)}$	$V^{(n)}$
$^{27}_{13}$Al	3.09 ± 0.08	0.0163 ∓ 0.003	0.0169 ∓ 0.003
$^{142}_{58}$Ce	6.00 ± 0.10	0.0844 ∓ 0.0067	0.117 ∓ 0.008
$^{208}_{82}$Pb	6.86 ± 0.09	0.0575 ∓ 0.0066	0.107 ∓ 0.008

TABLE IV. Same as Table I, but here the results of the analysis of the proton scattering experiments are used for the neutron density distribution [24,25] (method 3 in Sec. III A).

Nucleus	D	$S^{(p)}$	$V^{(p)}$	$S^{(n)}$	$V^{(n)}$
$^{12}_{6}$C	0.0074	0.0032	0.0032	0.0031	0.0032
$^{48}_{22}$Ti	0.0870	0.0371	0.0399	0.0462	0.0495
$^{58}_{28}$Ni	0.130	0.0548	0.0605	0.0606	0.0667
$^{90}_{40}$Zr	0.176	0.0715	0.0844	0.0841	0.100
$^{208}_{82}$Pb	0.156	0.0457	0.0812	0.0712	0.122

on the assumed functional form. Since the skin type distribution is assumed in Ref. [23], there may be errors associated with this assumption.

We have shown that in method 3 the ambiguity of $S^{(n)}$ and $V^{(n)}$ is reduced to a few percent even for heavy nuclei such as lead (Pb) if we use the results of the new experiment. The neutron distributions derived from experiments depend on how we treat the scattering of a proton and a nucleus, so that there might be uncertainties in the evaluation of $S^{(n)}$ and $V^{(n)}$ associated with the validity of the scattering theory. Improvement of scattering theory would be necessary to give a more realistic error estimation [30].

C. Numerical evaluation of conversion rate

It is now straightforward to evaluate the conversion rate through Eq. (14) once a theoretical model with LFV is specified. In this subsection, we present a μ-e conversion branching ratio for various types of LFV interaction in order to show the possibility of discriminating the different models through the Z dependence. We also compare our results with existing calculations for the case where the photonic dipole operators are nonvanishing.

We consider the following three cases.

(1) The photonic dipole operators A_L and/or A_R are nonvanishing. The μ-e conversion branching ratio is given by

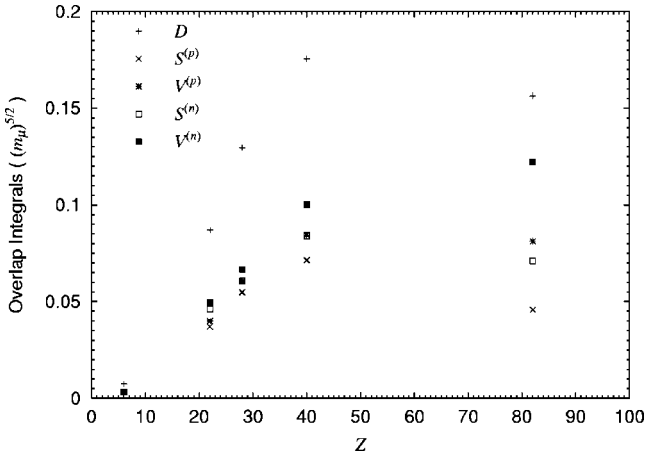

FIG. 7. Same as Fig. 3, but here the results of the analysis of the proton scattering experiments are used for the neutron density distribution [24,25] (method 3 in Sec. III A).

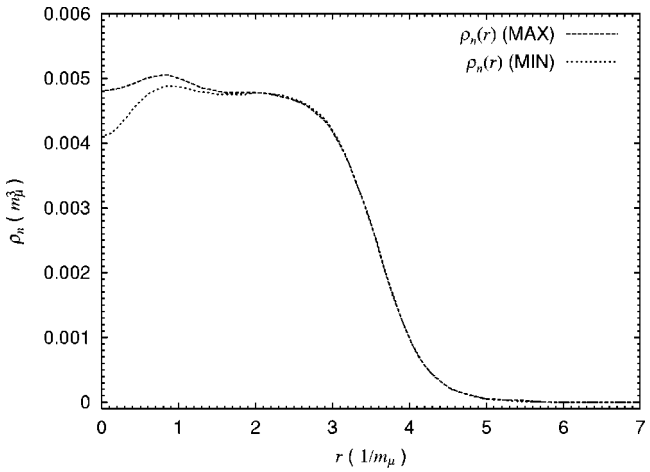

FIG. 8. The error envelope of the neutron density distribution for the $^{208}_{82}$Pb nucleus [28].

$$B_{\mu N\to eN}\equiv\frac{\omega_{\rm conv}}{\omega_{\rm capt}}=\frac{2G_{\rm F}^2D^2(|A_L|^2+|A_R|^2)}{\omega_{\rm capt}}, \tag{32}$$

where $\omega_{\rm capt}$ is the muon capture rate. For convenience, we list the capture rate in Appendix B [31].

(2) The scalar operators $g_{RS(d)}$ and/or $g_{LS(d)}$ are nonvanishing. The μ-e conversion branching ratio in this case is given by

$$B_{\mu N\to eN}=\frac{2G_{\rm F}^2(G_S^{(d,p)}S^{(p)}+G_S^{(d,n)}S^{(n)})^2(|g_{LS(d)}|^2+|g_{RS(d)}|^2)}{\omega_{\rm capt}}. \tag{33}$$

(3) The vector operators $g_{RV(u)}$ and $g_{LV(u)}$ satisfy $g_{RV(u)}=-2g_{RV(d)}\neq 0$ and/or $g_{LV(u)}=-2g_{LV(d)}\neq 0$. The μ-e conversion branching ratio in this case is given by

$$B_{\mu N\to eN}=\frac{2G_{\rm F}^2V^{(p)2}(|\tilde{g}_{LV}^{(p)}|^2+|\tilde{g}_{RV}^{(p)}|^2)}{\omega_{\rm capt}}. \tag{34}$$

The first case appears to be a good approximation in SUSY models for many cases, especially in SO(10) SUSY

TABLE V. Maximum and minimum values of the overlap integrals for the neutron density distribution, which is changed within the error envelope.

		$S^{(n)}$	$V^{(n)}$	Reference
$^{40}_{20}$Ca	Minimum	0.0331	0.0352	[26]
	Maximum	0.0338	0.0359	
$^{58}_{28}$Ni	Minimum	0.0584	0.0644	[26]
	Maximum	0.0592	0.0651	
$^{116}_{50}$Sn	Minimum	0.0958	0.120	[26]
	Maximum	0.104	0.128	
$^{208}_{82}$Pb	Minimum	0.0679	0.120	[27]
	Maximum	0.0789	0.131	

TABLE VI. Maximum and minimum values of the overlap integrals for the neutron density distribution for $^{208}_{82}$Pb based on the analysis in Ref. [28].

		D	$S^{(p)}$	$V^{(p)}$	$S^{(n)}$	$V^{(n)}$	Reference
$^{208}_{82}$Pb	Minimum	0.163	0.0493	0.0845	0.0675	0.0119	[28]
	Maximum	0.163	0.0493	0.0845	0.0697	0.0121	

GUT models [4] and in SUSY models with right-handed neutrinos [6]. The second case is realized in some cases of SUSY models with R-parity violation [3]. The third case corresponds to the situation where the monopole form factors give dominant contributions in the μ-e-γ transition. The μ-e conversion branching ratios are shown for three cases in Figs. 9 (method 1), 10 (method 2), and 11 (method 3). In these figures the branching ratios are normalized by the value for aluminum evaluated by method 1: namely,

$$\text{Dipole:}\quad B_{\mu N\to eN}(Z=13)=9.9(|A_L|^2+|A_R|^2), \tag{35}$$

$$\text{Scalar:}\quad B_{\mu N\to eN}(Z=13)=1.7\times10^2(|g_{LS(d)}|^2+|g_{RS(d)}|^2), \tag{36}$$

$$\text{Vector:}\quad B_{\mu N\to eN}(Z=13)=2.0(|\tilde{g}^{(p)}_{LV}|^2+|\tilde{g}^{(p)}_{RV}|^2). \tag{37}$$

We can see that, for all three types, the branching ratio increases with Z for $Z\lesssim30$, is largest for $30\lesssim Z\lesssim60$, and decreases for $Z\gtrsim60$. It is also seen that the conversion ratios are very different in heavy nuclei depending on the type of interaction. From this property we may be able to distinguish models beyond the SM through several experiments with different targets.

In order to see the improvements of the present method over older calculations, we compare three different approximations for the case where the photonic dipole operators are nonvanishing: namely, our calculation, the Weinberg-Feinberg approximation, and the approximation by Shanker. For this purpose we define the ratio $R(Z)\equiv B_{\mu N\to eN}/B(\mu\to e\gamma)$, where the $\mu\to e\gamma$ branching ratio $B(\mu\to e\gamma)$ is given by $384\pi^2(|A_L|^2+|A_R|^2)$. The present method thereby gives

$$R(Z)=\frac{G_F^2D^2}{192\pi^2\omega_{\rm capt}}. \tag{38}$$

In the Weinberg-Feinberg calculation, the relativistic effects and the Coulomb distortion were ignored [12]. We define the conversion branching ratio $B^{\rm WF}_{\mu N\to eN}$ and the ratio of ratios $R^{\rm WF}(Z)$ in the Weinberg-Feinberg approximation by the following formulas:

$$B^{\rm WF}_{\mu N\to eN}=\frac{8G_F^2m_\mu^5}{\pi^2}\alpha^3Z_{\rm eff}^4ZF_p^2(|A_L|^2+|A_R|^2)\frac{1}{\omega_{\rm capt}}, \tag{39}$$

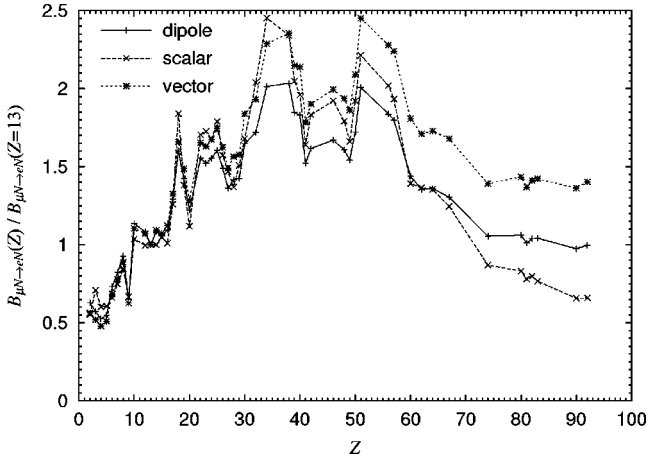

FIG. 9. The μ-e conversion ratios for typical theoretical models are plotted as functions of the atomic number Z. The solid, the long dashed, and the dashed lines represent the cases where the photonic dipole, scalar, and vector operators dominate, respectively. The proton and neutron distributions are taken according to method 1 in Sec. III A, and the conversion ratios are normalized by the conversion ratio in aluminum nuclei ($Z=13$).

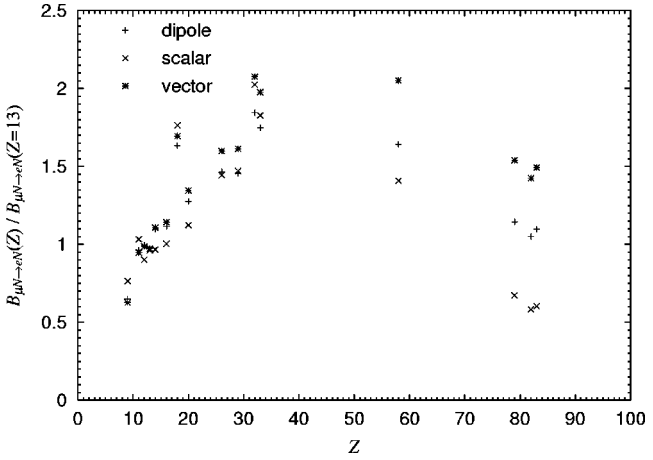

FIG. 10. The μ-e conversion ratios for typical theoretical models evaluated by method 2 in Sec. III A. The branching ratio is normalized by $B_{\mu N\to eN}(Z=13)$ evaluated by method 1.

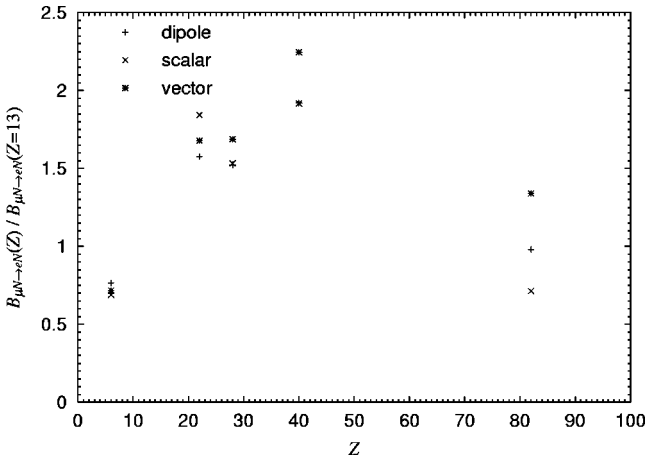

FIG. 11. The μ-e conversion ratios for typical theoretical models evaluated by method 3 in Sec. III A. The branching ratio is normalized by $B_{\mu N\to eN}(Z=13)$ evaluated by method 1.

TABLE VII. The model parameters of the proton density functions are listed. These values are extracted from Refs. [20]. The abbreviations HO, 2pF, 3pF, 2pG, 3pG, FB, and SOG represent the harmonic oscillator model, the two-parameter Fermi model, the three-parameter Fermi model, the two-parameter Gaussian model, the three-parameter Gaussian model, the Fourier-Bessel expansion, and the sum of Gaussians, respectively. We do not list here parameters for FB and SOG expansions; see Ref. [20].

Nucleus	Model	c_p or a_p (fm)	z_p (fm) or α	w_p	Nucleus	Model	c_p or a_p (fm)	z_p (fm) or α	w_p
$^{4}_{2}$He	SOG	—	—	—	$^{80}_{34}$Se	2pG	4.622	2.365	—
$^{7}_{3}$Li	HO	1.77	0.327	—	$^{88}_{38}$Sr	FB	—	—	—
$^{9}_{4}$Be	HO	1.791	0.611	—	$^{89}_{39}$Y	2pF	4.86	0.542	—
$^{11}_{5}$B	HO	1.69	0.811	—	$^{90}_{40}$Zr	FB	—	—	—
$^{12}_{6}$C	FB	—	—	—	$^{93}_{41}$Nb	2pF	4.953	0.541	—
$^{14}_{7}$N	3pF	2.570	0.5052	−0.180	$^{98}_{42}$Mo	FB	—	—	—
$^{16}_{8}$O	FB	—	—	—	$^{110}_{46}$Pd	FB	—	—	—
$^{19}_{9}$F	2pF	2.59	0.564	—	$^{114}_{48}$Cd	2pF	5.314	0.571	—
$^{20}_{10}$Ne	3pF	2.791	0.698	−0.168	$^{115}_{49}$In	2pF	5.357	0.563	—
$^{24}_{12}$Mg	3pF	2.791	0.698	−0.168	$^{120}_{50}$Sn	3pG	5.110	2.619	0.292
$^{27}_{13}$Al	FB	—	—	—	$^{121}_{51}$Sb	2pF	5.32	0.57	—
$^{28}_{14}$Si	3pF	3.340	0.580	−0.233	$^{138}_{56}$Ba	3pG	5.3376	2.6776	0.3749
$^{31}_{15}$P	FB	—	—	—	$^{139}_{57}$La	2pF	5.71	0.535	—
$^{32}_{16}$S	FB	—	—	—	$^{142}_{60}$Nd	2pF	5.839	0.569	—
$^{35}_{17}$Cl	3pF	3.476	0.599	−0.10	$^{152}_{62}$Sm	FB	—	—	—
$^{40}_{18}$Ar	FB	—	—	—	$^{158}_{64}$Gd	FB	—	—	—
$^{39}_{19}$K	3pF	3.743	0.585	−0.201	$^{165}_{67}$Ho	2pF	6.12	0.57	—
$^{40}_{20}$Ca	FB	—	—	—	$^{166}_{68}$Er	3pF	5.98	0.446	0.19
$^{48}_{22}$Ti	FB	—	—	—	$^{181}_{73}$Ta	2pF	6.38	0.64	—
$^{51}_{23}$V	2pF	3.91	0.532	—	$^{184}_{74}$W	2pF	6.51	0.535	—
$^{52}_{24}$Cr	FB	—	—	—	$^{197}_{79}$Au	2pF	6.38	0.535	—
$^{55}_{25}$Mn	2pF	3.89	0.567	—	$^{204}_{80}$Hg	FB	—	—	—
$^{56}_{26}$Fe	3pG	3.505	2.325	0.380	$^{205}_{81}$Tl	SOG	—	—	—
$^{59}_{27}$Co	2pF	4.158	0.575	—	$^{208}_{82}$Pb	FB	—	—	—
$^{58}_{28}$Ni	FB	—	—	—	$^{209}_{83}$Bi	FB	—	—	—
$^{63}_{29}$Cu	2pF	4.218	0.596	—	$^{232}_{90}$Th	2pF	6.851	0.518	—
$^{64}_{30}$Zn	3pG	3.664	2.425	0.342	$^{238}_{92}$U	2pF	6.874	0.556	—
$^{74}_{32}$Ge	FB	—	—	—					

$$R^{\mathrm{WF}}(Z)=\frac{B^{\mathrm{WF}}_{\mu N\to eN}}{B(\mu\to e\gamma)}=\frac{G_{\mathrm{F}}^2 m_\mu^5\alpha^3 Z_{\mathrm{eff}}^4 Z F_p^2}{48\pi^4\omega_{\mathrm{capt}}}. \tag{40}$$

Notice that these are not exactly the same as the formulas given in the original paper because they used approximate formulas for the capture rate and the form factors for the general photonic transition. Shanker improved the Weinberg-Feinberg formula by taking into account the relativistic effects and the Coulomb distortion. In his approximation, the branching ratio and the ratio of ratios for the dipole photonic interaction are given by

$$B^{\mathrm{S}}_{\mu N\to eN}=128e^2G_{\mathrm{F}}^2V^{(p)2}(|A_L|^2+|A_R|^2)\frac{1}{\omega_{\mathrm{capt}}}, \tag{41}$$

$$R^{\mathrm{S}}(Z)=\frac{B^{\mathrm{S}}_{\mu N\to eN}}{B(\mu\to e\gamma)}=\frac{e^2G_{\mathrm{F}}^2V^{(p)2}}{3\pi^2\omega_{\mathrm{capt}}}. \tag{42}$$

We present our $R(Z)$, $R^{\mathrm{WF}}(Z)$, and $R^{\mathrm{S}}(Z)$ in Fig. 12. Here we used the proton density in method 1 and the muon capture rate ω_{capt} from the experiments [31]. We see that the three quantities have similar Z dependence: they range from 0.002 to 0.006, and are largest for $Z=30$–60. The values of $R^{\mathrm{WF}}(Z)$ and $R^{\mathrm{S}}(Z)$ are larger than our $R(Z)$ by 30% for $Z\gtrsim 50$. We have reproduced with good accuracy the result by Czarnecki *et al.*, where they evaluated $R(Z)$ for aluminum (Al), titanium (Ti), and lead (Pb) nuclei. Kosmas obtained in Ref. [17] the result that $R(Z)$ is a monotonically increasing function, but he did not take into account the Coulomb distortion effect. We could indeed obtain the increasing function of $R(Z)$ by ignoring this effect. Thus the Coulomb distortion effect of the wave function is important in the calculation of the conversion rate for heavy nuclei, as noted by Shanker [14].

IV. SUMMARY

We calculated the coherent μ-e conversion rate for general LFV interactions for various nuclei. We used updated nuclear data for proton and neutron distributions and took into account the ambiguity associated with the neutron dis-

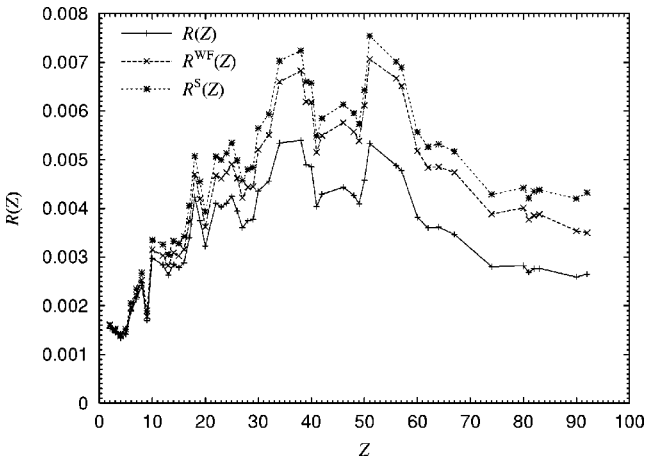

FIG. 12. The μ-e conversion branching ratio divided by the $\mu \to e\gamma$ decay branching ratio for method 1 is plotted as a function of atomic number Z. The solid line $[R(Z)]$, the long-dashed line $[R^{\mathrm{WF}}(Z)]$, and the dashed line $[R^{\mathrm{S}}(Z)]$ represent the results of our calculation, the Weinberg-Feinberg formula, and Shanker's approximation, respectively.

tribution. We gave the list of overlap integrals in Tables I, II, and IV for various nuclei, from which we can calculate conversion rates for general interactions for LFV using Eq. (14). We also investigated the Z dependence of the conversion rate. We saw that the branching ratio increases for the light nuclei such as $Z \lesssim 30$, is largest for $Z = 30$–60, and decreases for heavy nuclei with $Z \gtrsim 60$. Although this tendency of the Z dependence is the same for different types of coupling constants, there are significant differences in the Z dependence of the branching ratios. We showed that the ambiguity in the calculation of the overlap integrals associated with proton densities (D, $S^{(p)}$, and $V^{(p)}$) is quite small because the charge densities of the nuclei are well known. On the other hand, the overlap integrals $S^{(n)}$ and $V^{(n)}$ contain uncertainty from the neutron distribution, especially for heavy nuclei. We estimated $S^{(n)}$ and $V^{(n)}$ with several inputs. Using the neutron density distribution determined from proton scattering experiments performed in the 1970s and pionic atom experiments, we showed that the conversion rate changes by 20%–30% for heavy nuclei. Adopting the improved neutron density distribution determined by the new proton scattering experiment, we found that the ambiguity is significantly reduced down to a few percent. Because the main ambiguity for heavy nuclei is associated with the neutron density, it will be possible to make a precise prediction if we can determine the neutron density with improved analysis and experiments.

The results of our calculation are useful in choosing the appropriate target nuclei for future experiments for the μ-e conversion search. In addition, it may be possible to identify the theoretical models beyond standard model through the Z dependence of different interactions when the signal of μ-e conversion is experimentally observed.

ACKNOWLEDGMENTS

We would like to thank J. Hisano for useful discussions. This work was supported by the JSPS (R.K. and M.K.). The work of Y.O. was supported in part by a Grant-in-Aid of the Ministry of Education, Culture, Sports, Science and Technology, Government of Japan (No. 13640309), priority area ''Supersymmetry and Unified Theory of Elementary Particles'' (No. 707).

TABLE VIII. The total capture rates used in calculation are listed [31].

Nucleus	ω_{capt} (10^6 s^{-1})	Nucleus	ω_{capt} (10^6 s^{-1})
$^{4}_{2}$He	0.000336	$^{72}_{32}$Ge	5.569
$^{7}_{3}$Li	0.0018	$^{75}_{33}$As	6.104
$^{9}_{4}$Be	0.0074	$^{88}_{38}$Sr	7.02
$^{11}_{5}$B	0.0219	$^{89}_{39}$Y	7.89
$^{12}_{6}$C	0.0388	$^{90}_{40}$Zr	8.66
$^{14}_{7}$N	0.0693	$^{93}_{41}$Nb	10.36
$^{16}_{8}$O	0.1026	$^{92}_{42}$Mo	9.614
$^{19}_{9}$F	0.229	$^{110}_{46}$Pd	10.00
$^{20}_{10}$Ne	0.200	$^{114}_{48}$Cd	10.61
$^{23}_{11}$Na	0.3772	$^{115}_{49}$In	11.40
$^{24}_{12}$Mg	0.4841	$^{120}_{50}$Sn	10.44
$^{27}_{13}$Al	0.7054	$^{121}_{51}$Sb	10.21
$^{28}_{14}$Si	0.8712	$^{138}_{56}$Ba	9.94
$^{31}_{15}$P	1.1185	$^{139}_{57}$La	10.71
$^{32}_{16}$S	1.352	$^{140}_{58}$Ce	11.60
$^{35}_{17}$Cl	1.333	$^{142}_{60}$Nd	12.50
$^{40}_{18}$Ar	1.30	$^{152}_{62}$Sm	12.22
$^{39}_{19}$K	1.849	$^{158}_{64}$Gd	11.82
$^{40}_{20}$Ca	2.557	$^{165}_{67}$Ho	12.95
$^{48}_{22}$Ti	2.59	$^{166}_{68}$Er	13.04
$^{51}_{23}$V	3.069	$^{181}_{73}$Ta	12.86
$^{52}_{24}$Cr	3.472	$^{184}_{74}$W	12.36
$^{55}_{25}$Mn	3.857	$^{197}_{79}$Au	13.07
$^{56}_{26}$Fe	4.411	$^{205}_{81}$Tl	13.90
$^{59}_{27}$Co	4.940	$^{207}_{82}$Pb	13.45
$^{58}_{28}$Ni	5.932	$^{209}_{83}$Bi	13.10
$^{63}_{29}$Cu	5.676	$^{232}_{90}$Th	13.1
$^{64}_{30}$Zn	5.834	$^{238}_{92}$U	12.4

APPENDIX A: PROTON AND NEUTRON DENSITIES IN NUCLEI

We introduce the models of the nucleon densities in nuclei and list the values of the parameters of these models used in the calculation.

We used one of the following models for each nucleus [20].

(1) Harmonic oscillator model (HO):

$$\rho_{p(n)}(r) = \rho_0 \left[1 + \alpha \left(\frac{r}{a} \right)^2 \right] \exp\left[- \left(\frac{r}{a} \right)^2 \right]. \tag{A1}$$

(2) Two-parameter Fermi model (2pF):

$$\rho_{p(n)}(r) = \frac{\rho_0}{1 + \exp[(r - c_{p(n)})/z_{p(n)}]}. \tag{A2}$$

(3) Three-parameter Fermi model (3pF):

$$\rho_{p(n)}(r)=\frac{\rho_0(1+w_{p(n)}r^2/c_{p(n)}^2)}{1+\exp[(r-c_{p(n)})/z_{p(n)}]}. \tag{A3}$$

(4) Two-parameter Gaussian model (2pG):

$$\rho_{p(n)}(r)=\frac{\rho_0}{1+\exp[(r^2-c_{p(n)}^2)/z_{p(n)}^2]}. \tag{A4}$$

(5) Three-parameter Gaussian model (3pG):

$$\rho_{p(n)}(r)=\frac{\rho_0(1+w_{p(n)}r^2/c_{p(n)}^2)}{1+\exp[(r^2-c_{p(n)}^2)/z_{p(n)}^2]}. \tag{A5}$$

Here $c_{p(n)}$, $z_{p(n)}$, and $w_{p(n)}$ are the model parameters and ρ_0 is the normalization constant. We also used the following model-independent analysis for several nuclei.

(6) The Fourier-Bessel (FB) expansion:

$$\rho_{p(n)}(r)=\begin{cases}\sum_v a_v j_0(v\pi r/R) & \text{for } r\leqslant R,\\ 0 & \text{for } r>R,\end{cases} \tag{A6}$$

where a_v are the coefficients, R is the cutoff radius, and the function $j_0(z)=\sin z/z$ is the spherical Bessel function of zeroth order.

(7) The sum of Gaussians expansion (SOG):

$$\rho_{p(n)}(r)=\sum_i A_i\left\{\exp\left[-\left(\frac{r-R_i}{\gamma}\right)^2\right]+\exp\left[-\left(\frac{r+R_i}{\gamma}\right)^2\right]\right\}, \tag{A7}$$

where

$$A_i=\frac{ZeQ_i}{2\pi^{3/2}\gamma^3(1+2R_i^2/\gamma^2)}. \tag{A8}$$

We list the models and their parameters used in calculation in Table VII. We do not list parameters for the FB and SOG expansions there; see Ref. [20].

APPENDIX B: MUON CAPTURE RATE IN NUCLEI

We list in Table VIII the muon capture rates ω_{capt} that are used in our calculation [31].

[1] For review, see Y. Kuno and Y. Okada, Rev. Mod. Phys. **73**, 151 (2001).

[2] A.E. Faraggi and M. Pospelov, Phys. Lett. B **458**, 237 (1999); R. Kitano, *ibid.* **481**, 39 (2000).

[3] J.E. Kim, P. Ko, and D.G. Lee, Phys. Rev. D **56**, 100 (1997); K. Huitu, J. Maalampi, M. Raidal, and A. Santamaria, Phys. Lett. B **430**, 355 (1998); A. Faessler, T.S. Kosmas, S. Kovalenko, and J.D. Vergados, Nucl. Phys. **B587**, 25 (2000); A. de Gouvêa, S. Lola, and K. Tobe, Phys. Rev. D **63**, 035004 (2001).

[4] R. Barbieri, L.J. Hall, and A. Strumia, Nucl. Phys. **B445**, 219 (1995).

[5] R. Barbieri and L.J. Hall, Phys. Lett. B **338**, 212 (1994); J. Hisano, T. Moroi, K. Tobe, and M. Yamaguchi, *ibid.* **391**, 341 (1997); **397**, 357(E) (1997); Y. Okada, K.I. Okumura, and Y. Shimizu, Phys. Rev. D **58**, 051901 (1998); **61**, 094001 (2000).

[6] F. Borzumati and A. Masiero, Phys. Rev. Lett. **57**, 961 (1986); J. Hisano, T. Moroi, K. Tobe, M. Yamaguchi, and T. Yanagida, Phys. Lett. B **357**, 579 (1995); J. Hisano, T. Moroi, K. Tobe, and M. Yamaguchi, Phys. Rev. D **53**, 2442 (1996); J. Hisano, D. Nomura, and T. Yanagida, Phys. Lett. B **437**, 351 (1998); J. Hisano, D. Nomura, Y. Okada, Y. Shimizu, and M. Tanaka, Phys. Rev. D **58**, 116010 (1998); J. Hisano and D. Nomura, *ibid.* **59**, 116005 (1999); W. Buchmuller, D. Delepine, and F. Vissani, Phys. Lett. B **459**, 171 (1999); J. Ellis, M.E. Gómez, G.K. Leontaris, S. Lola, and D.V. Nanopoulos, Eur. Phys. J. C **14**, 319 (2000); W. Buchmuller, D. Delepine, and L.T. Handoko, Nucl. Phys. **B576**, 445 (2000); J. Sato, K. Tobe, and T. Yanagida, Phys. Lett. B **498**, 189 (2001); J. Sato and K. Tobe, Phys. Rev. D **63**, 116010 (2001); A. Kageyama, S. Kaneko, N. Shimoyama, and M. Tanimoto, Phys. Lett. B **527**, 206 (2002); J.R. Ellis, J. Hisano, S. Lola, and M. Raidal, Nucl. Phys. **B621**, 208 (2002).

[7] MEGA Collaboration, M.L. Brooks *et al.*, Phys. Rev. Lett. **83**, 1521 (1999).

[8] L. M. Barkov *et al.*, research proposal to PSI; S. Ritt, in *Proceedings of the 2nd International Workshop on Neutrino Oscillations and their Origin*, edited by Y. Suzuki *et al.* (World Scientific, Singapore, 2000), p. 245.

[9] P. Wintz, in *Proceedings of the First International Symposium on Lepton and Baryon Number Violation*, edited by H. V. Klapdor-Kleingrothaus and I. V. Krivosheina (Institute of Physics, Bristol, 1998), p. 534.

[10] MECO Collaboration, M. Bachman *et al.*, Experimental Proposal E940 to Brookhaven National Laboratory AGS, 1997.

[11] Y. Kuno, in *Proceedings of the 2nd International Workshop on Neutrino Oscillations and their Origin* [8], p. 253.

[12] S. Weinberg and G. Feinberg, Phys. Rev. Lett. **3**, 11 (1959).

[13] W.J. Marciano and A.I. Sanda, Phys. Rev. Lett. **38**, 1512 (1977).

[14] O. Shanker, Phys. Rev. D **20**, 1608 (1979).

[15] A. Czarnecki, W.J. Marciano, and K. Melnikov, hep-ph/9801218; in *Workshop on Physics at the First Muon Collider and at the Front End of the Muon Collider*, edited by S. H. Geer and R. Raja, AIP Conf. Proc. No. 435 (AIP, Woodbury, NY, 1998), p. 409.

[16] H.C. Chiang, E. Oset, T.S. Kosmas, A. Faessler, and J.D. Vergados, Nucl. Phys. **A559**, 526 (1993); T.S. Kosmas, J.D. Vergados, O. Civitarese, and A. Faessler, *ibid.* **A570**, 637 (1994); T.S. Kosmas and J.D. Vergados, Phys. Rep. **264**, 251 (1996); T.S. Kosmas, J.D. Vergados, and A. Faessler, Phys. At. Nucl.

61, 1161 (1998); T. Kosmas, Z. Ren, and A. Faessler, Nucl. Phys. **A665**, 183 (2000); T. Siiskonen, J. Suhonen, and T.S. Kosmas, Phys. Rev. C **62**, 035502 (2000).
[17] T.S. Kosmas, nucl-th/0108045.
[18] M. E. Rose, *Relativistic Electron Theory* (John Wiley, New York, 1961).
[19] T.S. Kosmas, S. Kovalenko, and I. Schmidt, Phys. Lett. B **511**, 203 (2001).
[20] C.W. De Jager, H. De Vries, and C. De Vries, At. Data Nucl. Data Tables **36**, 495 (1987); G. Fricke *et al.*, *ibid.* **60**, 177 (1995).
[21] C. J. Batty, E. Friedman, H. J. Gils, and H. Rebel, in *Advances in Nuclear Physics*, edited by J. W. Negele, and E. Vogt (Plenum Press, New York, 1989), Vol. 19, p. 1.
[22] A. Trzcińska, J. Jastrzębski, P. Lubiński, F.J. Hartmann, R. Schmidt, T. von Egidy, and B. Kłos, Phys. Rev. Lett. **87**, 082501 (2001).
[23] C. Garcia-Recio, J. Nieves, and E. Oset, Nucl. Phys. **A547**, 473 (1992).
[24] L. Ray, G.W. Hoffmann, G.S. Blanpied, W.R. Coker, and R.P. Liljestrand, Phys. Rev. C **18**, 1756 (1978).
[25] G. Pauletta *et al.*, Phys. Lett. **106B**, 470 (1981).
[26] L. Ray, Phys. Rev. C **19**, 1855 (1979).
[27] G.W. Hoffmann *et al.*, Phys. Rev. C **21**, 1488 (1980).
[28] V.E. Starodubsky and N.M. Hintz, Phys. Rev. C **49**, 2118 (1994).
[29] A.M. Mack *et al.*, Phys. Rev. C **52**, 291 (1995).
[30] S. Karataglidis, K. Amos, B.A. Brown, and P.K. Deb, Phys. Rev. C **65**, 044306 (2002).
[31] T. Suzuki, D.F. Measday, and J.P. Roalsvig, Phys. Rev. C **35**, 2212 (1987).